ACS APPLIED MATERIALS & INTERFACES

Research Article

www.acsami.org

Hydrogen Ion Supercapacitor: A New Hybrid Configuration of Highly Dispersed MnO_2 in Porous Carbon Coupled with Nitrogen-Doped Highly Ordered Mesoporous Carbon with Enhanced H-Insertion

Deyu Qu,[†] Jianfeng Wen,[†] Dan Liu,[†] Zhizhong Xie,[†] Xuran Zhang,[†] Dong Zheng,[‡] Jiahen Lei,[†] Wei Zhong,[†] Haolin Tang,*[,§] Liang Xiao,[†] and Deyang Qu*[,‡]

[†]Department of Chemistry, School of Chemistry, Chemical Engineering and Life Science and [§]State Key Laboratory of Advanced Technology for Materials Synthesis and Processing, Wuhan University of Technology, Wuhan 430070, Hubei, P. R. China

[‡]Department of Chemistry, University of Massachusetts Boston, 100 Morrissey Boulevard, Boston, Massachusetts 02125, United States

ABSTRACT: A new configuration of hydrogen ion supercapacitors was reported. A positive electrode composed of pseudocapacitive MnO_2, highly dispersed into active porous carbon through an impregnation method, was combined with a nitrogen-doped highly ordered mesoporous carbon with enhanced electrochemical hydrogen insertion capacity as a negative electrode. During the operation, hydrogen ion shuttled between MnO_2 and carbon electrodes. The MnO_2 was formed on the surface of nanostructured carbon through a spontaneous redox reaction. Operating in an aqueous neutral solution, the hybrid device demonstrated an extended working voltage to ~2.1 V with good cycle life.

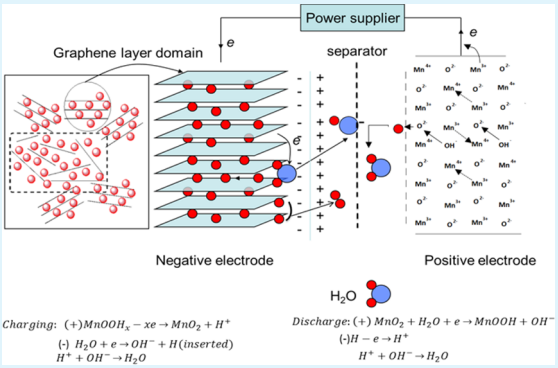

KEYWORDS: *hydrogen ion supercapacitor, pseudocapacitive MnO_2 electrode, highly ordered mesoporous carbon, electrochemical hydrogen insertion*

1. INTRODUCTION

Supercapacitors and secondary batteries are now considered to be the two major advanced energy storage devices. Secondary batteries are well-known to have high energy density but relative low power density and limited cycle-life. On the other hand, supercapacitors can provide very high power density with long cycle-life. But the low energy density narrowed the supercapacitor application area. To fill in the gaps between these two systems, a new system was suggested where a battery electrode is coupled with a supercapacitor electrode to form a hybrid device. This hybrid configuration ensures the supply of high energy density as well as high power density. Various rechargeable battery electrodes or pseudocapacitance materials have been launched into this system, such as $Ni(OH)_2$, MnO_2, MoO_3, V_2O_5, TiO_2, $LiMn_2O_4$, $Li_4Ti_5O_{12}$, and graphite.[1−20] However, to increase the energy density by bringing the Faradaic electrode into the system will result in the cost of recyclability.[4,21,22] To alleviate this problem, a H-insertion carbon electrode was introduced into the hybrid supercapacitor.[21,22] Because the inserted protons are from the water, high recyclability is achieved. The use of an aqueous solution is useful not only as a source of protons through electrolysis of water, but also has the merits of high ionic conductivity, high safety, low cost, and convenient operation in air, to name a few. But the water decomposition on the carbon materials limits the operating potential of H-insertion hybrid supercapacitor to ~1.1 V. Apparently this also restricts the energy density, since $E = 1/2CV^2$, where E, C, V represent energy, capacitance, and voltage, respectively. To improve the energy density of the hybrid device by widening the electrochemical window, a pseudocapacitive MnO_2 electrode is introduced into the system to replace the double-layer capacitive active carbon. Compared to previous systems, the introduction of MnO_2 can shift the oxygen evolution potential more positive, increase the device operating voltage and provide much higher capacitance. These all result in an increase of energy density to the system.

But before involving the MnO_2 pseudocapacitive electrode in the hybrid device, there are still several issues, such as low conductivity and mechanic instability with the MnO_2 electrode, which must be resolved. It has been demonstrated that the use of nanoscale MnO_2 incorporated with conductive materials, like porous carbon materials, can improve their capacitance, conductivity, and recyclability.[4,16,18−20,23−48] There were two methods to incorporate MnO_2 into the carbon: mechanical mixing and impregnation.[49] To deposit nanosized MnO_2 directly on the surface of the nanostructures within carbon, the impregnation method, a spontaneous redox reaction of

Received: October 3, 2014
Accepted: December 2, 2014
Published: December 2, 2014

potassium permanganate ($KMnO_4$) with active carbon materials, was applied in this study.[16,18,19,25,27,32,33,49−51] As demonstrated in previous reports, nitrogen-doped highly ordered mesoporous carbon (N-HOMC) can provide enhanced hydrogen insertion capacity as well as high double-layer capacitance due to the surface-bound groups and ordered mesostructure.[52,53] This carbon material was used as the negative electrode to couple with the homogeneously formed MnO_2/active carbon (AC) electrode. In this study, the characterization and electrochemical properties of MnO_2/AC electrode were investigated. The performances of MnO_2/H-insertion hybrid devices were also presented. Note that, in the present study, neutral electrolyte was used instead of 30% KOH solution. Since MnO_2 exhibits pseudocapacitance in mild aqueous solutions and hydrogen, adsorption and diffusion into the carbon matrix is found to be favored over hydrogen evolution in pH neutral condition.[54,55] To achieve better performance, Na_2SO_4 solution was used in this study.[24]

2. EXPERIMENTAL SECTION

Triblock poly(ethylene oxide)-*b*-poly(propylene oxide)-*b*-poly(ethylene oxide) copolymers Pluronic F127 (EO106 PO70 EO106, Mav = 12 600) were purchased from Sigma-Aldrich Corp. Other chemicals were purchased from Sinopharm Chemical Reagent Corp. All chemicals were used as received without further purification. The preparation of N-HOMC has been reported elsewhere.[52,53] 1 mol of resorcinol, 0.5 mol of hexamethylenetetramine(HMT), 0.0159 mol of triblock poly(ethylene oxide)-*b*-poly(propylene oxide)-bpoly(ethylene oxide) copolymers Pluronic F127, 0.33 mol of 1,3,5-trimethylbenzene (TMB), 2.7 mol of aqueous ammonia (28 wt %), and 300 mol of deionized water were mixed and stirred for 1 h at room temperature and for 24 h at 80 °C. Then the product was collected and calcined at 900 °C for 3 h under nitrogen atmosphere. The synthesized N-HOMC was then activated. First, the mixtures of carbon material and KOH with 1:4 mass ratios were dispersed in ethanol under stirring. After the ethanol was removed through an evaporation step at 60 °C under ultrapure argon atmosphere with stirring, the activation was then initiated by heating the sample at 700 °C for 90 min in ultrapure argon atmosphere. The resulting mixtures, after being cooled to room temperature, were washed by enough 1 M HCl solution and deionized water. Finally, the sample was dried at 100 °C for 12 h. Before use, all the carbon materials, including activated N-HOMC and AC, were reflux-washed with acetone in a Soxhlet extractor for ∼24 h to remove the physically bonded surface functional groups. The MnO_2/AC electrode was prepared by reacting $KMnO_4$ with active carbon. First, a certain amount of activated carbon was mixed with 1 M Na_2SO_4 solution at 50 °C and then stirred with 0.1 M $KMnO_4$ solution for 3 h under ultrapure argon atmosphere. The product was then washed with deionized water and dried at 80 °C in vacuum for 24 h.

Transmission electron microscopy (TEM) images were taken with a JEM 2100F electron microscope operating at 200 kV. Scanning electron microscopy (SEM) images were taken using a Hitachi S-4800 field emission scanning electron microscope. Powder X-ray diffraction (XRD) patterns were recorded on a Rigaku D/MAX-RB diffractometer with a Cu Kα radiation operating at 40 kV, 50 mA. X-ray photoelectron (XP) spectra were obtained using a VG Multilab 2000 X-ray photoelectron spectrometer with a Mg KR radiation. Narrow-scan spectra of the C 1s, O 1s, and Mn 2p regions were obtained with 15 eV pass energy, 100 W electron-beam power, and a resolution of 0.1 eV. Binding energy was calibrated with a C 1s peak at 284.6 eV. A Micromeritics ASAP 2020 porosimeter was used for the surface area and porosity measurements. Nitrogen was used as absorbent gas. Density function theory (DFT) software from Micromeritics was also used. A PerkinElmer 3300DV inductively coupled plasma spectrometer (ICP) was used for ICP measurements.

To make the electrode, the N-HOMC or MnO_2/AC materials (85 wt %) were mixed with carbon black (10 wt %) and Teflon suspension (5 wt % of dry material). After thoroughly mixing, those pastes were left to air-dry. The resulting Teflon-bonded material was rolled into a thin film, and then the electrode was punched out of film with geometric surface area of 1 cm^2. The disc electrode with overall mass of 10 mg was then sandwiched into two pieces of nickel foam current collector.

1 M Na_2SO_4 solution was used as electrolyte in all measurements. An AutoLab electrochemical workstation (PGSTAT100N) was used for impedance measurements. Electrochemical impedance spectroscopy (EIS) was carried out at the frequency region from 0.001 Hz to 100 kHz with amplitude of 5 mV. A CH Instruments 660D electrochemical workstation was used for electrochemical measurements. A saturated calomel electrode (SCE) reference electrode was used in all measurements. A National Instruments USB-6212 data acquisition card controlled by Labview software was used to monitor the potential change for the individual negative (N-HOMC) and positive (MnO_2/AC) electrodes against reference electrode during the charge/discharge process.

3. RESULTS AND DISCUSSION

The formation of MnO_2 within AC was investigated by X-ray photoelectron spectroscopy (XPS) measurements. Figure 1A−C shows the XP spectra of the synthesized MnO_2-loaded active carbon material in the region of C 1s, O 1s, and Mn 2p, respectively. Figure 1C shows that the binding energy of Mn $2p_{3/2}$ and Mn $2p_{1/2}$ peaks are 642.2 and 653.9 eV, respectively. This 11.8 eV spin-energy separation agrees well with previous results reported for MnO_2 and indicates the formation of MnO_2 in this study.[23,25] The relative molar ratio of Mn and O was estimated by[56]

$$C_{Mn}/C_O = (A_{Mn}/R_{Mn})/(A_O/R_O)$$

where A is the peak area and R is the atom sensitivity factor. Using R_{Mn} and R_O of 2.15 and 0.63, respectively,[56] the ratio of Mn to O (C_{Mn}/C_O) was found to be 1:2. This further confirms the existence of MnO_2. The oxidation state of Mn was analyzed through the O 1s spectrum.[23,25] The binding energy of O 1s peak, found at 531.6 eV, is best fit with the three peaks as shown in Figure 1B. The positions of these three peaks are 529.8, 531.4, and 532.8 eV, which can be assigned to Mn−O−Mn bond for tetravalent oxide, Mn−O−H bond for hydrated trivalent oxide, and H−O−H bond for residual water, respectively. The average Mn valence in MnO_2 can then be calculated by[23]

$$\text{Mn oxidation state} = 4*(S_{Mn-O-Mn} - S_{Mn-O-H}) + 3*S_{Mn-O-H}/S_{Mn-O-Mn}$$

where S is the intensity of the different components in O 1s spectrum. In this study, the average Mn valence in MnO_2 was found to be less than 3.5. Apparently the actual chemical formula for the manganese oxide compound was $MnOOH_x$ (x < 1); this intermediate valence made the reversible surface redox reaction between Mn^{3+} and Mn^{4+} within MnO_2 faster. The amount of MnO_2 deposited into AC material was determined to be 54 wt % by means of an ICP spectrometer.

The phase of the MnO_2 formed on active carbon substrate was characterized by XRD. Figure 2 shows the XRD patterns of formed MnO_2/AC material. The broad diffraction peaks that appeared at 37° and 66° can be indexed to an amorphous brinessite-type α-MnO_2 (JCPDS 42−1317),[15,19,25,29] where other peaks near 25°, 42°, and 79° were from active carbon materials.

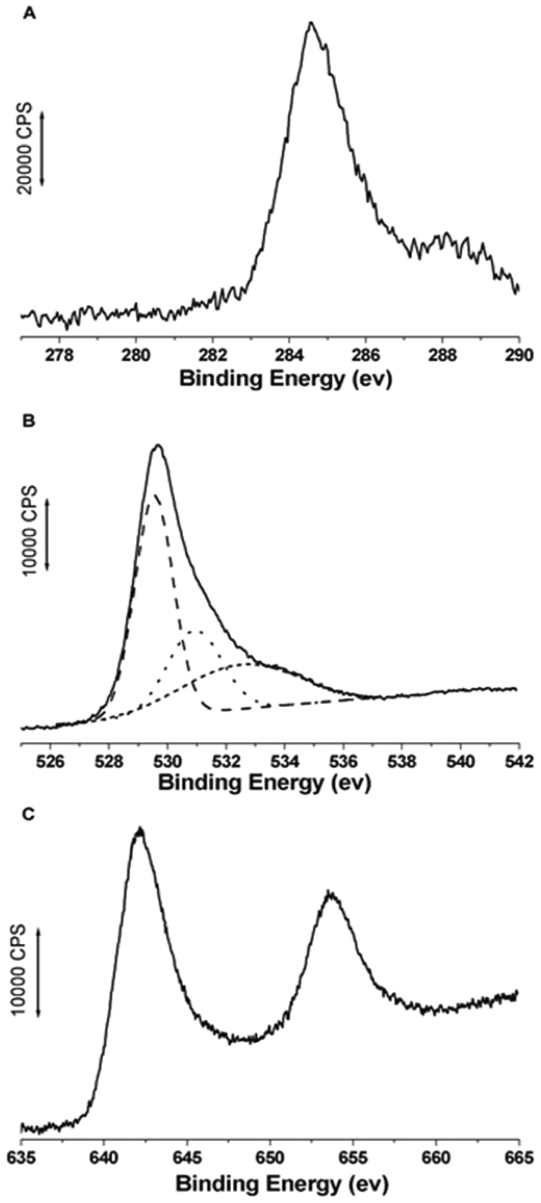

Figure 1. XP spectra of prepared MnO_2/AC in the region (A) C 1s, (B) O 1s, and (C) Mn 2p.

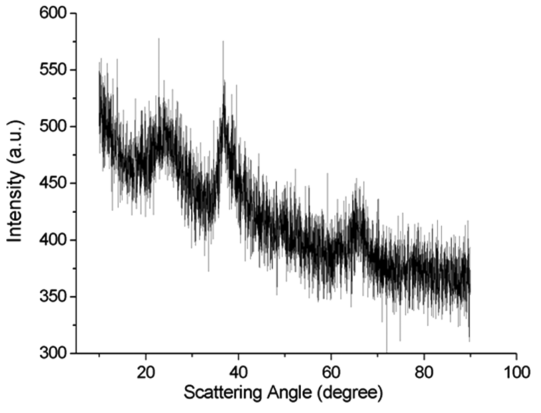

Figure 2. XRD patterns of prepared MnO_2/AC.

The surface structure of the MnO_2/AC material was also characterized. Figure 3 shows the SEM and energy-dispersive spectrometry (EDS) images of the MnO_2/AC material. The EDS images clearly show that the MnO_2 are highly dispersed within the active carbon material. This indicated that the spontaneous redox reaction of $KMnO_4$ with active carbon yielded well-distributed MnO_2 within the porous carbon support. The MnO_2 homogeneously coated onto the nanostructures within carbon was also proven by the porous distribution. Figure 4 shows the comparison of the DFT pore size distributions (PSDs) for the AC and MnO_2/AC materials. It clearly shows that, after MnO_2 was deposited onto the carbon, the surface area contribution from micropores within the active carbon significantly decreased. But the macro- and mesoporous structures were almost identical before and after the deposited MnO_2. This suggested that, in the course of MnO_2 formation, the MnO_4^- ions might diffuse into the micropores within AC first and then react with carbon and form MnO_2 coating on the inner surface of those micropores. The highly distributed MnO_2 within the internal micropores in AC made the porous carbon materials a three-dimensional current collector for pseudocapacitive MnO_2.[23] This configuration provided a high electrochemical activated interface by imbedding the intrinsically poor conductor, MnO_2, in a conductive carbon matrix that can also facilitate the rapid electrolyte transport to MnO_2 phase.

Figure 5 shows the alternating current (ac) impedance spectra of AC and MnO_2/AC electrodes. In both cases, two distinct sections are observed in the Nyquist plot: a semicircle at high frequency region, which corresponds to a parallel combination of charge-transfer resistance (R_{ct}) and capacitance, and a relatively straight line in the low frequency region, which can be attributed to ion diffusion into the porous structure of carbon electrode. An equivalent circuit, shown inside Figure 5, was used for the numerical fittings for the spectra. It can be observed that this model simulates the spectra very well. It was found that the R_{ct} and capacitance for MnO_2/AC were higher than those for AC, indicating the relative poor conductivity and high pseudocapacitance of MnO_2 materials. Note that a constant phase element (CPE), instead of a capacitor, is used in parallel with R_{ct} in the equivalent circuit to compensate for the nonhomogeneity of the porous electrode. This demonstrates the existence of a rough and porous surface in both electrodes.

The ionic diffusion through the porous structure of both electrodes was also investigated in the low frequency region. A finite-length Warburg element was used to represent this process. It is well-known that a Warburg element occurs when a charge carrier diffuses through a medium. Lower frequencies correspond to diffusion deeper into the medium. If the medium is thin or the diffusion path is short enough, low frequencies will penetrate the entire thickness, creating a finite-length Warburg element. Since the finite-length Warburg component fits the ac impedance spectrum well, it demonstrates that the MnO_2 coating is highly dispersed within the nanostructure of active carbon.

As for the negative electrode materials, N-HOMC was synthesized following the previous study, and its hydrogen insertion enhancement property has been investigated.[52,53] Figure 6 shows the SEM and TEM images of synthesized N-HOMC in this study. They are all similar to results in previous reports indicating the formation of a fiber-like carbon material with a highly ordered mesoporous structure.[52,53]

The electrochemical performances of both the positive and negative electrode as well as the hybrid device were evaluated.

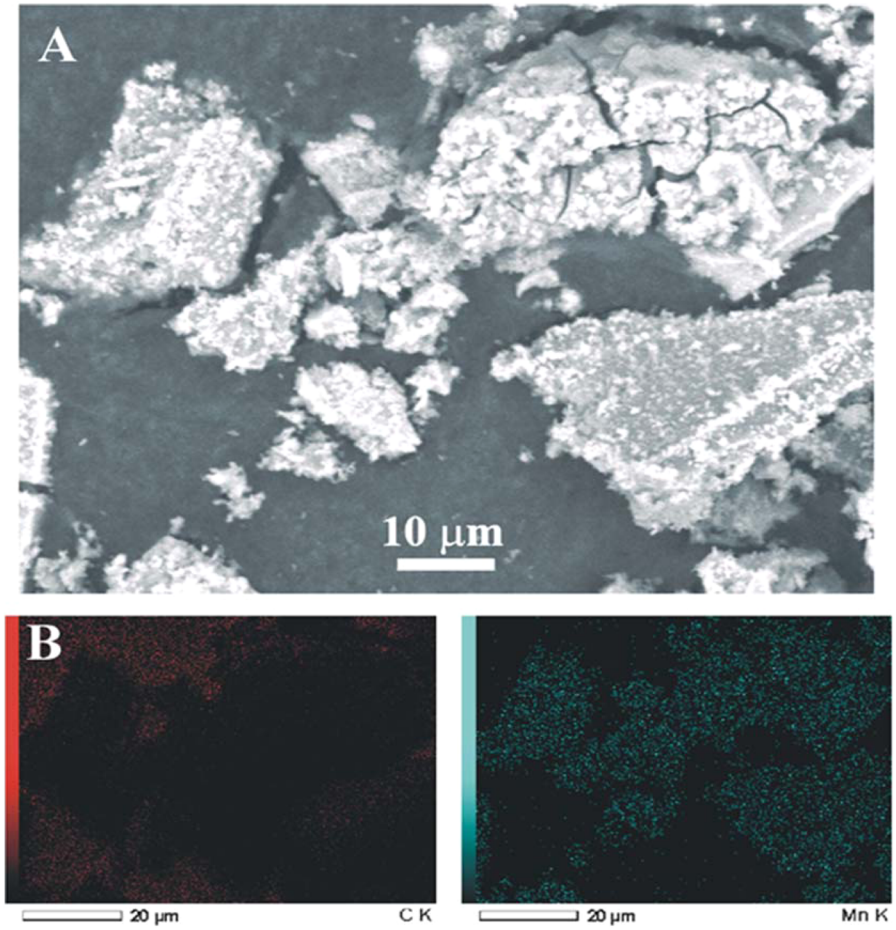

Figure 3. (A) SEM; (B) full scan EDS (left: Carbon; right: Mn) image for prepared the MnO_2/AC electrode.

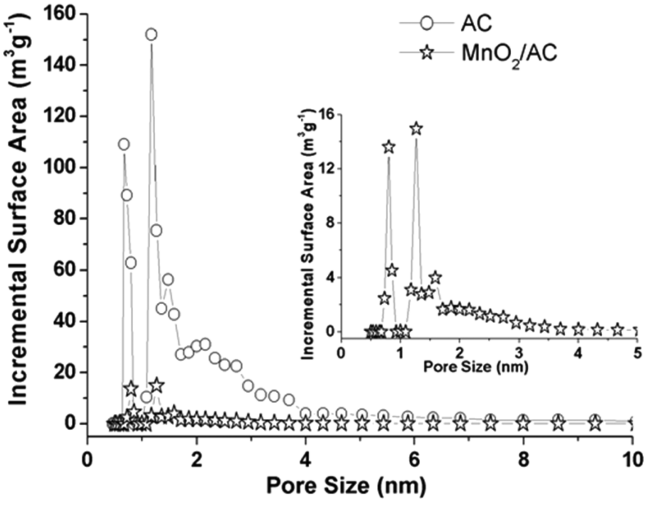

Figure 4. Comparison of the pore size distributions for activated carbon and MnO_2/AC materials.

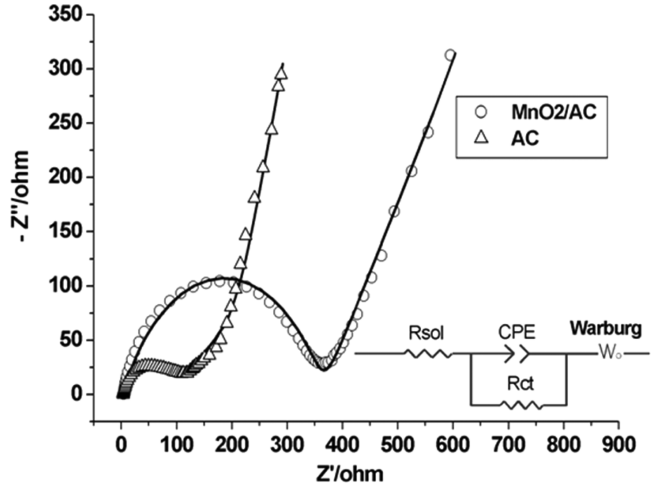

Figure 5. AC impedance spectra and fitting results (solid line) of MnO_2/AC electrode (○) and AC electrode (△) in 1 M Na_2SO_4 solution. (inset) The equivalent circuit used for the fitting of the ac impedance spectra.

At first, the electrochemical properties and potential windows of N-HOMC and MnO_2/AC electrodes were examined by cyclic voltammetry (CV) measurements. Figure 7 shows the CVs of N-HOMC and MnO_2/AC measured at 5 mV s^{-1} with potential windows of −1.2 to 0.5 V and 0 to 0.9 V, respectively. A relatively rectangular shape CV can be observed, which indicated the good double-layer capacitive behavior for N-HOMC electrode and nearly ideal pseudocapacitive behavior for MnO_2/AC electrode. The capacitances for N-HOMC and MnO_2/AC electrode are calculated to be ∼120 F g^{-1} and 340 F g^{-1}, respectively. As for the distortion in both CV curves at their edges of the potential window, this was attributed to the oxygen evolution reaction (ORR) arising on both electrodes at their positive limit voltage as well as hydrogen evolution reaction occurring on N-HOMC and Mn^{4+} irreversible

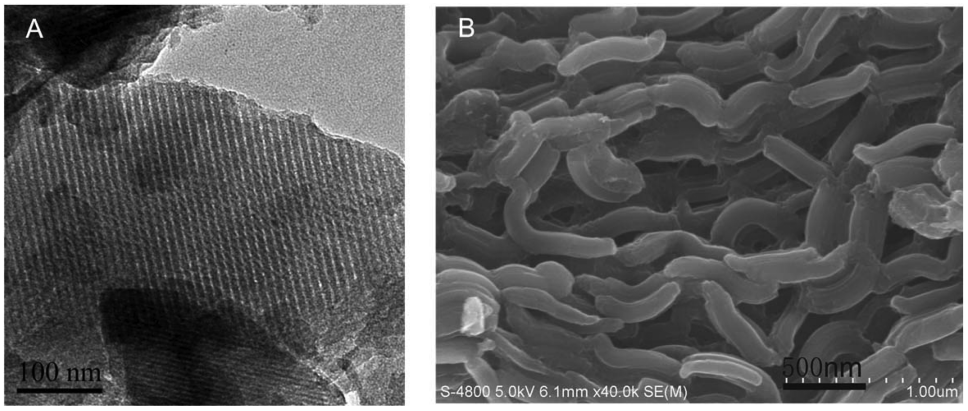

Figure 6. TEM image (A), high magnification SEM image (B) of N-HOMC.

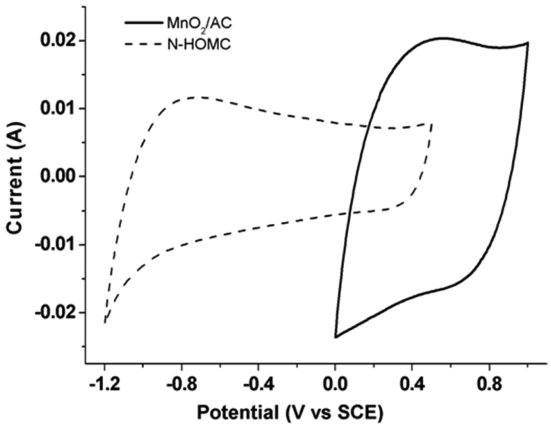

Figure 7. CV curves of N-HOMC(dash line) and MnO_2/AC(solid line) measured at 5 mV s^{-1} in 1 M Na_2SO_4 solution with potential windows of −1.2 to 0.5 V and 0 to 0.9 V, respectively.

reduction on MnO_2/AC at the negative limit voltage.[23] Obviously, the high overpotential of ORR upon MnO_2/AC will extend the operating voltage to ∼2.1 V in aqueous media after fabricating the hybrid cell with N-HOMC as the negative electrode and MnO_2/AC as the positive electrode.

Figure 8 shows the charge−discharge profiles of the positive (MnO_2/AC) and negative (N-HOMC) electrodes and the hybrid device with an applied current of 100 mA g^{-1} (per total mass of both positive and negative electrodes). As shown in Figure 8A, the potentials of the positive and negative electrodes were recorded separately against an SCE reference electrode in the course of charge/discharge of the hybrid device.

On the positive electrode side, two distinct regions can be observed in the charging curve. A short charging process for the double-layer building up on AC followed by a long linear charging curve for the H-desertion or the oxidation low oxidation state of Mn is observed. On the negative electrode side, three regions, which are related to double-layer charging process, electrochemical H-insertion process, and hydrogen evolution reaction, are shown in the potential curve as discussed in the previous reports.[22,53]

Figure 8B shows the comparison of the charge−discharge curves for two hybrid supercapacitors at 2 mA rate. The solid line presents the new hybrid configuration discussed in this study, which was assembled with the positive pseudocapacitive MnO_2/AC electrode and negative H-insertion N-HOMC electrode. The dashed line corresponds to the hybrid supercapacitor studied in previous report, which was fabricated with a positive double-layer capacitive carbon electrode and a negative H-insertion AC electrode with an optimized weight ratio of 6:1.[22] From the discharge curves, the capacitance of these two hybrid supercapacitors was found to be 40.8 mAh g^{-1} and 10.4 mAh g^{-1} (based on total mass of both positive and negative electrodes), respectively. It clearly demonstrated that the capacitance of the device assembled with N-HOMC and MnO_2/AC markedly increased by using a pseudocapacitive-type electrode and an electrode with enhanced H-insertion ability. This result showed that, in comparison with the H-insertion/carbon hybrid configuration, not only the operating voltage of the hybrid supercapacitor extended form 1.1 to ∼2.1 V, but also the energy density increased more than 4 times. Figure 8C shows the capacitor discharged at various rate. Furthermore, the Coulombic efficiency for the hybrid device in this study is ∼86%, which is much higher than 46% reported previously for the one with double-layer and H-insertion electrodes. Note that the charge-storage mechanism was that the hydrogen ions moved from the negative electrode to positive electrode during discharge and back when charging. Such scheme of operation was very similar to that of Li-ion battery, except solid electrolyte interface (SEI) protective layer was not necessary for the current design since it was operated in an aqueous electrolyte. The detail mechanism is shown in Figure 9. During the charging process, the Mn ion in the host $MnOOH_x$ releases electrons, and H ions flow into the electrolyte, while the protons are simultaneously formed through H_2O electrolysis on the negative electrode and insert into the host carbon electrode. During discharge, the host negative electrode releases electrons, H ions flow back into the electrolyte, and the protons formed on the positive electrode from H_2O decomposition insert in the MnO_2 lattice.

Figure 10 shows the cycling stability of the hybrid device in a current rate of 100 mA g^{-1} (per total mass of both positive and negative electrodes). A capacitance was demonstrated for 150 cycles, indicating a good cycling stability. It should be pointed out that the mass ratio of positive MnO_2/AC electrode and negative N-HOMC electrode was not optimized. As demonstrated before, the cell potential can be adjusted through changing the mass ratio of positive and negative electrode, so does the total capacity.[8,57,58] Therefore, to further improve the performance of the hybrid device, the cell balance has to be engineered. Such investigation is in progress and will be reported later. It is also worth emphasizing that the H-insertion into MnO_2 follows a homogeneous "electron−proton hopping"

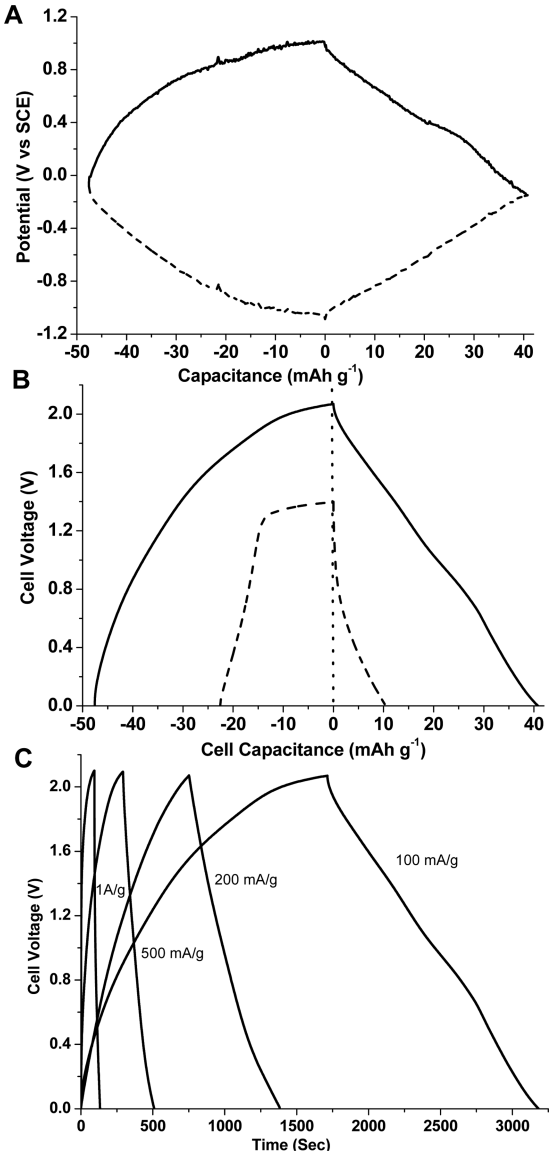

Figure 8. Charge−discharge curves (A) N-HOMC(dash line) and MnO_2/AC(solid line) electrodes vs SCE reference with an applied current of 100 mA g^{-1} (total mass of both electrodes); (B) hybrid supercapacitors composed by N-HOMC//MnO_2/AC with mass ratio of 1:1 (solid line) and AC//AC with mass ratio of 6:1(dash line) under applied current of 2 mA in 1 M Na_2SO_4 solution; and (C) the hybrid capacitor discharged at various rate.

mechanism.[59] As a result of electron exchange between Mn^{4+} and Mn^{3+} in the lattice the position of Mn^{3+}, not the manganese ion itself, can move around in the entire lattice. At the same time, protons from the H_2O electrochemical decomposition on the electrode surface are introduced into the lattice forming OH^- from O^{2-} in the lattice. Since the O−H bonds are broken due to the rotation and vibration, H^+ can hop from one O^{2-} to another. As long as the oxidation state of Mn is >3.5, the Jahn−Teller deformation can be avoided. The H-insertion process can take place reversibly without changing much of the original structure.[59]

4. CONCLUSION

A novel H-ion hybrid supercapacitor was developed here by fabricating a pseudocapacitive, highly dispersed MnO_2 within active porous carbon as a positive electrode and nitrogen-doped highly ordered mesoporous carbon with enhanced hydrogen-insertion capacity as a negative electrode. This device can be operated at a high voltage of 2.1 V in 1 M Na_2SO_4 aqueous solution and deliver an energy density of 40.8 mAh g^{-1} at current rate of 100 mA g^{-1} without trade-off recyclability.

AUTHOR INFORMATION

Corresponding Authors

*E-mail: thln@whut.edu.cn. (H.L.T.)
*E-mail: deyang.qu@umb.edu. (D.Y.Q.)

Notes

The authors declare no competing financial interest.

ACKNOWLEDGMENTS

This work was partially supported by the Natural Science Foundation of China (11474226 and 61274135) and Fundamental Research Funds for the Central Universities China (2014-zy-166 and 2014-LX-B1-11). The authors thank Dr. X.-Q. Liu for his assistance conducting TEM.

REFERENCES

(1) Amatucci, G. G.; Badway, F.; Pasquier, A. D. Intercalation Compounds for Battery Materials. *ECS Proc.* **2000**, *99*, 344−359.
(2) Amatucci, G. G.; Badway, F.; Pasquier, A. D.; Zheng, T. An Asymmetric Hybrid Nonoaqueous Energy Storage Cell. *J. Electrochem. Soc.* **2001**, *148*, A930−A939.
(3) Pasquier, A. D.; Plitz, I.; Gural, J.; Menocal, S.; Amatucci, G. G. Characteristics and Performance of 500 F Asymmetric Hybrid Advanced Supercapacitor Prototypes. *J. Power Sources* **2003**, *113*, 62−71.
(4) Simon, P.; Gogotsi, Y. Materials for Electrochemical Capacitors. *Nat. Mater.* **2008**, *7*, 845−854.
(5) Naoi, K.; Simon, P. New Material and New Configurations for Advanced Electrochemical Capacitors. *Electrochem. Soc. Interface* **2008**, *17*, 34−37.
(6) Burke, A. R&D Consideration for the Performance and Application of Electrochemical Capacitors. *Electrochim. Acta* **2007**, *53*, 1083−1091.
(7) Wang, H.; Yoshio, M. Graphite, A Suitable Positive Electrode Material for High-Energy Electrochemical Capacitors. *Electrochem. Commun.* **2006**, *8*, 1481−1486.
(8) Khomenko, V.; Raymundo-Pinero, E.; Beguin, F. High-Energy Density Graphite/AC Capacitor in Organic Electrolyte. *J. Power Sources* **2008**, *177*, 643−651.
(9) Tang, W.; Liu, L. L.; Tian, S.; Li, L.; Yue, Y. B.; Wu, Y. P.; Zhu, K. Aqueous Supercapacitors of High Energy Density Based on MoO_3 Nanoplates as Anode Material. *Chem. Commun.* **2001**, *47*, 10058−10060.
(10) Qu, Q. T.; Zhu, Y.; Gao, X. W.; Wu, Y. P. Core-Shell Structure of Polypyrrole Grown on V_2O_5 Nanoribbon as High Performance Anode Material for Supercapacitors. *Adv. Energy Mater.* **2012**, *2*, 950−955.
(11) Qu, Q. T.; Shi, Y.; Tran, S.; Chen, Y. H.; Wu, Y. P.; Holze, R. A New Cheap Asymmetric Aqueous Supercapacitor: Activated Carbon//$NaMnO_2$. *J. Power Sources* **2009**, *194*, 1222−1225.
(12) Qu, Q. T.; Li, L.; Tian, S.; Guo, W. L.; Wu, Y. P.; Holze, R. A Cheap Asymmetric Supercapacitor with High Energy at High Power: Activated Carbon//$K_{0.27}MnO_2{\cdot}0.6H_2O$. *J. Power Sources* **2010**, *195*, 2789−2794.
(13) Cericola, D.; Novák, P.; Wokaun, A.; Kotz, R. Hybridization of Electrochemical Capacitors and Rechargeable Batteries: An Experimental Analysis of the Different Possible Approaches Utilizing Activated Carbon, $Li_4Ti_5O_{12}$ and $LiMn_2O_4$. *J. Power Sources* **2011**, *196*, 10305−10313.

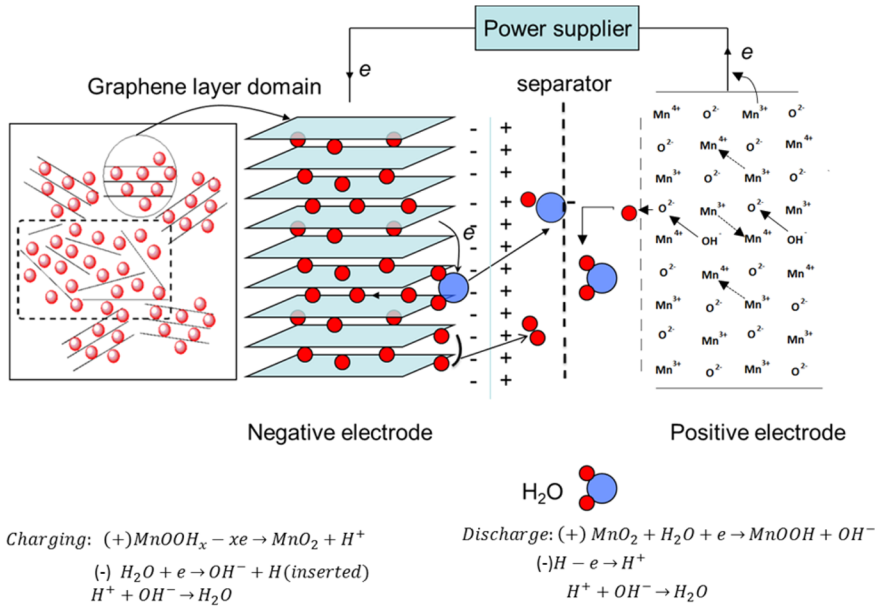

Figure 9. Mechanism of the H-ion supercapacitor.

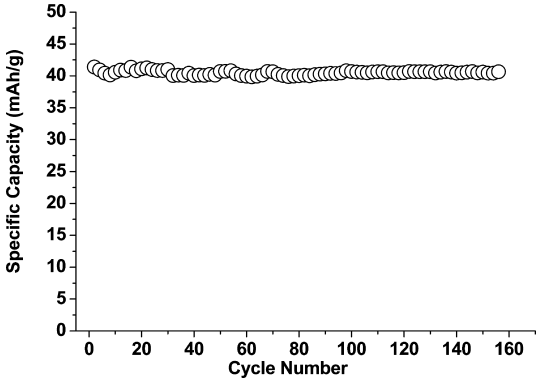

Figure 10. Cycling behavior of hybrid device assembled by N-HOMC and MnO_2/AC electrodes at a current rate of 100 m A g^{-1} (total mass of both electrodes).

(14) Tang, Z.; Tang, C.; Gong, H. A High Energy Density Asymmetric Supercapacitor from Nano-architectured $Ni(OH)_2$/Carbon Nanotube Electrodes. *Adv. Funct. Mater.* **2012**, *22*, 1272−1278.

(15) Fan, Z.; Yan, J.; Wei, T.; Zhi, L.; Ning, G.; Li, T.; Wei, F. Asymmetric Supercapacitors Based on Graphene/MnO_2 and Activated Carbon Nanofiber Electrodes with High Power and Energy Density. *Adv. Funct. Mater.* **2011**, *21*, 2366−2375.

(16) Yan, J.; Fan, Z.; Sun, W.; Ning, G.; Wei, T.; Zhang, Q.; Zhang, R.; Zhi, L.; Wei, F. Advanced Asymmetric Supercapacitors Based on $Ni(OH)_2$/Graphene and Porous Graphene Electrodes with High Energy Density. *Adv. Funct. Mater.* **2012**, *22*, 2632−2641.

(17) Wang, Q.; Wen, Z. H.; Li, J. H. A Hybrid Supercapacitor Fabricated with a Carbon Nanotubes Cathode and a TiO_2-B Nanowire Anode. *Adv. Funct. Mater.* **2006**, *16*, 2141−2146.

(18) Chen, L. F.; Huang, Z. H.; Liang, H. W.; Guan, Q. F.; Yu, S. H. Bacterial-cellulose-derived Carbon Nanofiber@MnO_2 and Nitrogen-doped Carbon Nanofiber Electrode Materials: An Asymmetric Supercapacitor with High Energy and Power Density. *Adv. Mater.* **2013**, *25*, 4746−4752.

(19) Yang, C.; Zhou, M.; Xu, Q. Three-dimensional Ordered Macroporous MnO_2/Carbon Nanocomposites as High-Performance Electrodes for Asymmetric Supercapacitors. *Phys. Chem. Chem. Phys.* **2013**, *15*, 19730−19740.

(20) Cao, J.; Wang, Y.; Zhou, Y.; Ouyang, J.-H.; Jia, D.; Guo, L. High Voltage Asymmetric Supercapacitor Based on MnO_2 and Graphene Electrodes. *J. Electroanal. Chem.* **2013**, *689*, 201−206.

(21) Qu, D.; Smith, P.; Gourdin, G.; Jiang, T.; Tran, T. A Hydrogen-insertion Asymmetric Supercapacitor. *Chem.—Eur. J.* **2012**, *18*, 3141−3143.

(22) Wang, L.; Zheng, D.; Qu, D.; Xiao, L.; Qu, D. Engineering Aspects of the Hybrid Supercapacitor with H-insertion Electrode. *J. Power Sources* **2013**, *230*, 66−69.

(23) Belanger, D.; Brousse, T.; Long, J. W. Manganese Oxides: Battery Materials Make the Leap to Electrochemical Capacitors. *Electrochem. Soc. Interface* **2008**, *17*, 49−52.

(24) Qu, Q. T.; Zhang, P.; Wang, B.; Chen, Y. H.; Tian, S.; Wu, Y. P.; Holze, R. Electrochemical Performance of MnO_2 Nanorods in Neutral Aqueous Electrolytes as a Cathode for Asymmetric Supercapacitors. *J. Phys. Chem. C* **2009**, *113*, 14020−14027.

(25) Wang, J.-G.; Yang, Y.; Huang, Z.-H.; Kang, F. A High-Performance Asymmetric Supercapacitor Based on Carbon and Carbon−MnO_2 Nanofiber Electrodes. *Carbon* **2013**, *61*, 190−199.

(26) Zhang, Y.; Li, J.; Kang, F.; Gao, F.; Wang, X. Fabrication and Electrochemical Characterization of Two-dimensional Ordered Nanoporous Manganese Oxide for Supercapacitor Applications. *Int. J. Hydrogen Energy* **2012**, *37*, 860−866.

(27) Peng, Y.; Chen, Z.; Wen, J.; Xiao, Q.; Weng, D.; He, S.; Geng, H.; Lu, Y. Hierarchical Manganese Oxide/Carbon Nanocomposites for Supercapacitor Electrodes. *Nano Res.* **2011**, *4*, 216−225.

(28) Chen, L.; Gu, N.; Ding, R.; Qi, L.; Wang, H. Facile Fabrication of Mesoporous Manganese Oxides as Advanced Electrode Materials for Supercapacitors. *J. Solid State Electrochem.* **2013**, *17*, 2579−2588.

(29) Shen, C.; Wang, X.; Li, S.; Wang, J.; Zhang, W.; Kang, F. A High-Energy-Density Micro Supercapacitor of Asymmetric MnO_2−Carbon Configuration by Using Micro-Fabrication Technologies. *J. Power Sources* **2013**, *234*, 302−309.

(30) Li, S.-M.; Wang, Y.-S.; Yang, S.-Y.; Liu, C.-H.; Chang, K.-H.; Tien, H.-W.; Wen, N.-T.; Ma, C.-C. M.; Hu, C.-C. Electrochemical Deposition of Nanostructured Manganese Oxide on Hierarchically Porous Graphene−Carbon Nanotube Structure for Ultrahigh-Performance Electrochemical Capacitors. *J. Power Sources* **2013**, *225*, 347−355.

(31) Zhao, Y.; Jiang, P.; Xie, S.-S. ZnO-template-mediated Synthesis of Three-dimensional Coral-like MnO_2 Nanostructure for Supercapacitors. *J. Power Sources* **2013**, *239*, 393−398.

(32) He, S.; Hu, C.; Hou, H.; Chen, W. Ultrathin MnO_2 Nanosheets Supported on Cellulose Based Carbon Papers for High-Power Supercapacitors. *J. Power Sources* **2014**, *246*, 754−761.
(33) Chen, D.; Song, M.-K.; Cheng, S.; Huang, L.; Liu, M. Contribution of Carbon Fiber Paper (CFP) to the Capacitance of a CFP-Supported Manganese Oxide Supercapacitor. *J. Power Sources* **2014**, *248*, 1197−1200.
(34) Hassan, S.; Suzuki, M.; Mori, S.; El-Moneim, A. MnO_2/Carbon Nanowalls Composite Electrode for Supercapacitor Application. *J. Power Sources* **2014**, *249*, 21−27.
(35) Boisset, A.; Athouël, L.; Jacquemin, J.; Porion, P.; Brousse, T.; Anouti, M. Comparative Performances of Birnessite and Cryptomelane MnO_2 as Electrode Material in Neutral Aqueous Lithium Salt for Supercapacitor Application. *J. Phys. Chem. C* **2013**, *117*, 7408−7422.
(36) Liu, M.; Gan, L.; Xiong, W.; Xu, Z.; Zhu, D.; Chen, L. Development of MnO_2/Porous Carbon Microspheres with a Partially Graphitic Structure for High Performance Supercapacitor Electrodes. *J. Mater. Chem. A* **2014**, *2*, 2555−2562.
(37) Huang, H.; Wang, X. Graphene Nanoplate-MnO_2 Composites for Supercapacitors: A Controllable Oxidation Approach. *Nanoscale* **2011**, *3*, 3185−3191.
(38) Cheng, Y.; Zhang, H.; Lu, S.; Varanasi, C. V.; Liu, J. Flexible Asymmetric Supercapacitors with High Energy and High Power Density in Aqueous Electrolytes. *Nanoscale* **2013**, *5*, 1067−1073.
(39) Tao, J.; Liu, N.; Li, L.; Su, J.; Gao, Y. Hierarchical Nanostructures of Polypyrrole@MnO_2 Composite Electrodes for High Performance Solid-state Asymmetric Supercapacitors. *Nanoscale* **2014**, *6*, 2922−2928.
(40) Xu, J.; Wu, H.; Xu, C.; Huang, H.; Lu, L.; Ding, G.; Wang, H.; Liu, D.; Shen, G.; Li, D.; Chen, X. Structural Engineering for High Energy and Voltage Output Supercapacitors. *Chem.—Eur. J.* **2013**, *19*, 6451−6458.
(41) Wang, C. C.; Chen, H. C.; Lu, S. Y. Manganese Oxide/Graphene Aerogel Composites as an Outstanding Supercapacitor Electrode Material. *Chem.—Eur. J.* **2014**, *20*, 517−523.
(42) Devaraj, S.; Gabriel, G. S.; Gajjela, S. R.; Balaya, P. Mesoporous MnO_2 and Its Capacitive Behavior. *Electrochem. Solid-State Lett.* **2012**, *15*, A57−A59.
(43) Jiang, R.; Cui, C.; Ma, H. Using Graphene Nanosheets as a Conductive Additive to Enhance the Capacitive Performance of α-MnO_2. *Electrochim. Acta* **2013**, *104*, 198−207.
(44) Kim, M.; Hwang, Y.; Min, K.; Kim, J. Introduction of MnO_2 Nanoneedles to Activated Carbon to Fabricate High-Performance Electrodes as Electrochemical Supercapacitors. *Electrochim. Acta* **2013**, *113*, 322−331.
(45) Mo, G.; Zhang, Y.; Zhang, W.; Ye, J. Design and Synthesis of Hierarchical Porous Electrode with Nanocomposites of MnO_2 Thin Layer Encapsulated Carbon Nanotubes and its Superb Charge Storage Characteristics. *Electrochim. Acta* **2013**, *113*, 373−381.
(46) Yang, S.; Cheng, K.; Huang, J.; Ye, K.; Xu, Y.; Cao, D.; Zhang, X.; Wang, G. High-Capacitance MnO_2 Nanoflakes on Preformed C/TiO_2 Shell/Core Nanowire Arrays for Electrochemical Energy Storage. *Electrochim. Acta* **2014**, *120*, 416−422.
(47) Song, Z.; Liu, W.; Zhao, M.; Zhang, Y.; Liu, G.; Yu, C.; Qiu, J. A Facile Template-free Synthesis of α-MnO_2 Nanorods for Supercapacitor. *J. Alloys Compd.* **2013**, *560*, 151−155.
(48) Zolfaghari, A.; Naderi, H. R.; Mortaheb, H. R. Carbon Black/Manganese Dioxide Composites Synthesized by Sonochemistry Method for Electrochemical Supercapacitors. *J. Electroanal. Chem.* **2013**, *697*, 60−67.
(49) Ominde, N.; Bartlett, N.; Yang, X.-Q.; Qu, D. The Effect of Oxygen Reduction on Activated Carbon Electrodes Loaded with Manganese Dioxide Catalyst. *J. Power Sources* **2008**, *185*, 747−753.
(50) Ominde, N.; Bartlett, N.; Yang, X.-Q.; Qu, D. Investigation of the Oxygen Reduction Reaction on the Carbon Electrodes Loaded with MnO2 Catalyst. *J. Power Sources* **2010**, *195* (13), 3984−3989.
(51) Wu, M.; Snook, G. A.; Chen, G. Z.; Fray, D. Redox Deposition of Manganese Oxide on Graphite for Supercapacitors. *Electrochem. Commun.* **2004**, *6*, 499−504.
(52) Liu, D.; Lei, J. H.; Guo, L. P.; Qu, D.; Li, Y.; Su, B. L. One-pot Aqueous Route to Synthesize Highly Ordered Cubic and Hexagonal Mesoporous Carbons from Resorcinol and Hexamine. *Carbon* **2012**, *50*, 476−487.
(53) Liu, D.; Zheng, D.; Wang, L.; Qu, D.; Xie, Z.; Lei, J.; Guo, L.; Deng, B.; Xiao, L.; Qu, D. Enhancement of Electrochemical Hydrogen Insertion in N-doped Highly Ordered Mesoporous Carbon. *J. Phys. Chem. C* **2014**, *118*, 2370−2374.
(54) Lee, H.; Goodenough, J. B. Supercapacitor Behavior with KCl Electrolyte. *J. Solid State Chem.* **1999**, *144*, 220−223.
(55) Chun, S.; Whitacre, J. F. Investigating the Role of Electrolyte Acidity on Hydrogen Uptake in Mesoporous Activated Carbons. *J. Power Sources* **2013**, *242*, 137−140.
(56) Wagner, C. D.; Riggs, W. D.; Davis, L. E.; Moulder, J. F.; Muileuberg, G. E. *Handbook of X-ray Photoelectron Spectroscopy;* PerkinElmer Corp.: Eden Prairie, MN, 1979.
(57) Ataherian, F.; Wu, N.-L. 1.2 V Manganese Oxide Symmetric Supercapacitor. *Electrochem. Commun.* **2011**, *13*, 1264−1267.
(58) Demarconnay, L.; Raymundo-Pinero, E.; Beguin, F. Adjustment of Electrodes Potential Window in an Asymmetric Carbon/MnO_2 Supercapacitor. *J. Power Sources* **2011**, *196*, 580−586.
(59) Qu, D. Y.; Bai, L.; Castledine, C. G.; Conway, B. E.; Adams, W. A. Spectro-electrochemcial Studies on Production and Role of Soluble Mn(III) Species in Discharge and Recharge of Various MnO_2 Cathode Materials. *J. Electroanal. Chem.* **1994**, *1*−*2*, 247−259.